Nanocomposite coatings for healing surface defects of glass fibers and improving interfacial adhesion

Shang-Lin Gao, Edith Mäder, Rosemarie Plonka

Nanocomposite coatings for healing surface defects of glass fibers and improving interfacial adhesion

Shang-Lin Gao, Edith Mäder, Rosemarie Plonka

PII: S0266-3538(07)00395-8
DOI: 10.1016/j.compscitech.2007.10.009
Reference: CSTE 3854

To appear in: *Composites Science and Technology*

Received Date: 20 September 2007
Accepted Date: 15 October 2007

Please cite this article as: Gao, S-L., Mäder, E., Plonka, R., Nanocomposite coatings for healing surface defects of glass fibers and improving interfacial adhesion, *Composites Science and Technology* (2007), doi: 10.1016/j.compscitech.2007.10.009

Nanocomposite coatings for healing surface defects of glass fibers and improving interfacial adhesion

Shang-Lin Gao, Edith Mäder, and Rosemarie Plonka

Leibniz Institute of Polymer Research, Dresden, Germany

ABSTRACT

Surface defects of brittle materials cause actual tensile strength much lower than the ultimate theoretical strength. Coatings can be used to 'heal' surface flaws and modify surface properties. Here, we describe an online process by which a nanometer-scale hybrid coating layer based on styrene-butadiene copolymer with single or muti-walled carbon nanotubes (SWCNTs, MWCNTs) and/or nanoclays, as mechanical enhancement and environmental barrier layer, is applied to alkali-resistant glass (ARG) and E-glass fibers. Our data indicates that the nanostructured and functionalised traditional glass fibers show significantly improved both mechanical properties and environmental corrosion resistance. With low fraction of nanotubes in sizing, the tensile and bending strength of healed glass fiber increases remarkably. No apparent strength variation appears for nanoclay coated fiber subjected to alkaline attack. We introduce a healing efficiency factor and conclude that the coating modulus, thickness and roughness are responsible for the mechanical improvement of fibers. Besides, nanocomposite coatings result in enhanced fiber/matrix interfacial adhesion, indicating nanotube related interfacial toughening mechanisms.

Keywords: *A. Coating, Glass fibers, Nanostructers, Nanocomposites*
B. Surface treatments, Strength, Interfacial strength
C. Crack, fiber bridging
D. Atomic force microscopy (AFM)

Corresponding author: *Dr. Edith Mäder*
Phone: *0351 4658 305*
Fax: *0351 4658 362*
e-mail: *emaeder@ipfdd.de*

1. Introduction

Most solid materials have surface defects. For glass and other brittle materials, surface defects cause the measured mechanical properties significantly lower than their theoretical values. The nanoscale surface defects providing extra stress at the tip of the cracks can lead to stress-corrosion cracking at low stress level, particularly in a humid environment. Our recent work showed that the surface critical flaws have size in a range of a few hundred nanometres which encouraged us to investigate whether the nano-reinforcements with similar size functions as a crucial role for healing [1, 2]. Healing nanoscale surface flaws and enhancing materials' lifetime by nanocoatings, therefore, are important for many traditional materials.

Reinforcement with nanomaterials is a topic of significant current interest. It is well known that surface defect-free and high purity carbon nanotubes have exceptional high Young's modulus and tensile strength. However, an efficient utilization of the excellent properties of nanoreinforcements to the microscopic and macroscopic level is a long standing problem. To date, the highest strength and Young's modulus reported in the literature are relatively disappointing: 1.8~3.2 GPa and ~ 40 GPa, respectively, for aligned nanotube composite bundles with very high volume loading of nanotubes (60 wt%) [3, 4], which are a factor of ten below those of the component individual nanotubes because of poor integration and weak interfacial adhesion. Therefore, to find an appropriate dispersion for the nanoreinforcements to increase volume concentration, limited by chemical inertness and van der Waals attractions, is not sufficient for producing high-quality composites. In contrast to this 'super-materials degraded by defects' approach, here, we apply a 'surface defects healed by super-materials' approach (Fig. 1), where the traditional alkali-resistant glass fibers (ARG) were coated using different nanostructured coating layers with low loading (<1 wt%) of single and multi walled carbon nanotubes (SWCNTs, MWCNTs) and/or organoclay to provide a protective layer against aqueous alkaline solution. AFM, SEM, TEM and single fiber tensile, bending and pull-out tests were used to investigate in detail the local surface topography, mechanical and interfacial properties.

2. Experimental

2.1 Materials

The control ARG with diameter of 17 m and E-glass fibers with diameter of 20~23 m utilized in this work were made at our institute. During the continuous spinning process, the ARG fibers were in-situ sized by an alkali-resistant sizing consisting of silane coupling agent, -aminopropyl-triethoxysilane, in conjunction with film formers in the aqueous sizing, namely S1. Additionally, either MWCNTs or nanoclay particles are dispersed in the epoxy film former

based sizing. The 0.2 wt% surface functionalized MWCNTs in the sizing were synthesized by an arc-discharge method (IFW, Germany) with an external diameter of 20-60 nm and a length of 100-1000 nm as described in Refs. [5, 6]. We applied additionally surface coatings to the control ARG using a commercial self-crosslinking styrene-butadiene copolymers (C2). The total weight gain due to the coatings is 5.3 wt% measured by pyrolysis (600 °C, 60 min) of the coated fibers. The 1 wt% organically modified silicates on the base of montmorillonite particles with a size of about 60 to 300 nm (Nanofil 15, Süd-Chemie AG, Moosburg, Germany) are dispersed in the obtained solution. A quaternary ammonium surfactant and a non-ionic surface active agent were added to the dispersion for homogeneous distribution of the constituents. We extracted the fibers in selected highly concentrated aqueous alkaline solution (5 wt % NaOH, pH of 14) at 20 °C for seven days, which is the most aggressive and corrosive condition to the fiber surface [1].

The E-glass fibers were also sized with aminosilane and maleic anhydride grafted PP film former dispersion containing less than 0.5 wt% nanotubes in the sizings. Simultaneously, thermoplastic polypropylene filaments with diameter of 26 m are manufactured from homopolymer PP (HD120M) and 2% Exxelor PO 1020 acts as the compatibiliser to improve the adhesion strength of the commingled yarns. This method of concentrating the nanomaterials in the sizing dispersion benefits from its ambient temperature treatment and environmentally friendly deposition, in addition to chemical versatility.

2.2 Characterization

Atomic force microscopy (AFM): An AFM (a Digital Instruments D3100, USA) was used as a surface morphology imaging tool to detect fiber, coatings and fracture surfaces. The topography and phase images of samples were studied in tapping mode, while phase shifts, i.e., changes in the phase angle of vibration with respect to the phase angle of the freely oscillating cantilever, recorded simultaneously with height changes, are present as a phase image. Its value depends on the energy dissipated in the tapping interaction of probe and specimen, which is normally sensitive to the surface and underlying structure of the specimens that could not be observed in the topography image due to variations in local elasticity and viscoelasticity, adhesion, hydrophilicity/hydrophobicity properties of the specimen [7-9]. The phase images reveal differences in these surface properties of the material which are currently only qualitative in nature. The cantilever (ULTRASHARP NSC16/50, MikroMasch, Estonia) has a normal spring constant of 35 N/m, a tip cone angle of 20 °, radius of 5~10 nm and modulus of 160 GPa to assure good imaging resolution. Specimens were prepared by fixing separate short fiber filaments on a silicon wafer, within a thin layer of pre-coated epoxy at the bottom side of the fiber.

Single-fiber tensile and bending test: The tensile strength of single fiber was measured using the Fafegraph Mechanical testing device (Fa. Textechno) equipped with a 10 N force cell. The gauge length is 20 mm and the cross velocity is 10 mm/min under 65 % relative humidity and 20°C according to specification EN ISO 5079. Based on a vibration approach, the diameter of each selected fiber was calculated from the fineness value, which was measured with a Vibromat ME (Fa. Textechno) according to specification EN ISO 53812 and ASTM D 1577. To verify the effect of surface properties on the statistical distribution of fiber tensile strength, the cumulative fracture probability *F* was fitted by single Weibull distribution model through the least squares method and the Weibull modulus m_o was calculated.

Due to the small dimensions of glass fiber, the bending strength is measured by means of a loop test [10]. The fiber is made into a loop which was forced between two parallel glass plates with distance of ten times of fiber diameter; at the same time, the fiber is attached to the jaws of the a self-made tensile testing machine which is mounted on an optical microscope. By pulling both ends of the fiber, the radius of curvature of the loop, *R*, decreases and eventually the fiber breaks due to bending; the smallest radius of curvature a fiber allow before breaking is recorded. For an isotropically elastic fiber with modulus of elasticity, *E*, and diameter, *d*, bent to a large radius of curvature (large with respect to fiber diameter), based on the simple bending theory under the assumption of linear elasticity, the failure bending moment, *M*, and maximum bending stress, $_{max}$ at outside of a curved fiber are

$$M = \frac{\pi d^4 E}{64R} \tag{1}$$

$$\sigma_{\max} = \frac{dE}{2R} \tag{2}$$

Single-fiber pull-out test (SFPO): Using embedding apparatus enabling PC-controlled temperature and time cycles, the model microcomposites for the single fiber pull-out test were prepared by accurately embedding the single fibers in matrix with embedding lengths of 100 through 200 µm. The pull-out test was carried out on a self-made pull-out apparatus with force accuracy of 1 mN and displacement accuracy of 0.07 µm with identical pull-out velocities (0.01 µm s^{-1}) at ambient temperature. The local interfacial adhesion strength, $_d$, and the critical interphase energy release rate, G_{ic}, can be determined by using the algorithm described previously [11].

3. Results and discussion

3.1 Nanocomposite coating morphology

We first examined the morphology of nanoreinforcements in coatings. Fig. 2 shows a pair of AFM topography/phase images of a nanocoating with nanotubes from identical areas captured on the glass fiber surface. Although it is normally impossible to observe the individual nanotube where it is embedded in thick coating polymer matrix, our phase image on the glass fiber surface where the coating layer is thin shows apparent contrast between the nanotube and polymer. The phase image qualitatively reveals a difference in coating surface or underlying material properties of the regions in terms of stiffness, viscosity and adhesion. According to the AFM observation at this region, the lengths of fibril multi-walled carbon nanotubes range between 20-300 nm, and the diameter about 20-40 nm (actually most tubes with lengths of ~100 nm and diameter of ~30 nm). There are still some residual nanoparticles/impurities observed after purification process, which is attributed to amorphous carbons, graphite and metal particles as a result of an arc-discharge processing method [12-14]. Interestingly, these short nanotubes show an irregular distribution and quite well separated from bundles which do not tend to normally agglomerate and close-packed patterns, suggesting that the high speed on-line sizing process could be utilized for separation of nanotube bundles for a wide range of composite applications.

The nanocomposite coatings with the nanometre-thin sheet-like layers of clay fillers are tested to function for moisture/gas barrier resistance and limit the diffusion of hydroxyl ions to glass surface and the crack tip. We have recently measured the sorption isotherms of fibers to understand the barrier levels achieved with in the coating [15]. The nanoclay containing coating has lower values of both adsorption and desorption than coating without clay at all ranges of relative pressure, suggesting that the clay coating adsorbs less water and the diffusion through the clay loaded coating appear much slower. Since a transport barrier layer affects both diffusion and sorption, a proposed mechanism of the improving alkali-resistance is that the clay particles retain water molecules and reduce the moisture adsorption and concentration in the coating layer and coating/fiber interface. The clay particles also act as obstacles forcing both outside solution molecules and inside dissolved alkali ions diffusing to long detours round the platelets (cf. Fig. 1). A number of experimental and theoretical studies of polymer film with clay have also shown that intrinsic permeability decrease significantly, i.e., the water diffusivity was reduced to half of its value in the neat polymer [16, 17]. Many approaches for predicting barrier properties have been discussed in literature [18-21] depending on the filler volume fraction, the aspect ratio and filler alignment. For efficient barrier characteristics at a low volume fraction of fillers (1%), the aspect ratio normally should be higher than 200. Additionally, taking into consideration of chemical effects of coating, as revealed by Zetapotential measurements in our early work [22], the acidic groups (i.e. COOH) of coating polymer were dominating on fiber surface before and after NaOH

treatment. Since the congruent dissolution of glass corrosion process is only valid in high pH environment, the coating with acidic character, as an alkali-deficient layer, can slow down the deterioration process by limiting the increase of the localized pH value and growth of silica gel layer. Therefore, the clay reinforced coating layer is rather alkali-resistant because of these different physico-chemical mechanisms.

3.2 Fiber tensile strength

We next investigated the tensile performance of the single fiber (Fig. 3a). In comparison with unsized samples, we observed a significant improvement of 70% of tensile strength for nanostructured ARG with nanotubes. The fiber strength also increased up to 40 % and 25 % for sized fiber and sized fiber with 1 wt% loading of organoclay in the sizing, respectively. The fiber fracture behaviour is strongly affected by the variation of sizing properties because the critical flaws which limit the strength of fibers are located at the surface. It is well known that the aminosilane sizing alone also accomplishes mechanical healing by formation of a cross-linked network, where the coupling agent can react at the glass surface with the hydrolysed silanol groups and favour the chemical coupling with the sizing as well as with the surrounding polymer matrix [23]. This strengthening effect is strongly depending on the coating chemical nature and roughness. One interesting observation in our previous work is that the maximum height roughness of fiber surface followed very closely the line predicted by the Griffith fracture criterion, which implies that good levelling of coatings is a prerequisite for fiber strengthening [22]. The fiber with nanoclay coatings, however, is heterogeneous associated with a higher surface roughness [2]. Importantly, the strength differences between the systems of sized and sized with clay might also be caused by the chemical nature of clay itself [24] or quaternary ammonium surfactant and a non-ionic surface active agent during process which affect adversely the formation of a cross-linked network. The varied breaking strength of glass fiber can be attributed to the distribution in flaw severity along the fiber length, where micro-cracks can be inherent to the glass itself or a result of the manufacturing process and handling of the fiber. Interestingly, as shown in Fig. 3b, both the Weibull plot lines and Weibull modulus, m_o, of coated systems shifts to higher values than those of the control. This indicates that the strength-controlling surface defects have lower heterogeneity distribution and the size of defects is reduced after healing. In other words, the healed flaws on the coated fibers show similar flaw size, severity and homogeneity compared to those on the control fibers.

Additionally, the effects of alkaline attacks on the average fiber strength are also compared in Fig. 3a. It is evident that sample of clay coatings would not yield a significant strength reduction upon alkali treatment. However, a significant strength reduction for systems with

sizings and nanotube sizings occurred. This can be partly compensated by an additional styrene-butadiene coating with carboxylic groups, which show an enhanced alkali-resistance as determined by the marginal strength reduction. Therefore, the durability and alkali-resistance are also improved, particularly the fiber with organoclay coatings. Overall, the coated fibers have higher strength values than the control one after alkaline corrosion, reflecting the improved environmental durability for fibers with nanostructured coatings.

Potential mechanisms include the contributions of different factors for the mechanical property improvement by reducing the fiber surface flaw formation and crack growth. Note that the polymer coatings have Young's moduli that are typically several orders of magnitude lower than the glass fiber, and therefore do not bear a significant portion of the mechanical load. Although the polymer coatings do not increase strength, they have the important function of protecting the glass surface from abrasion and chemical damage, which in turn would degrade glass fiber strength. The coating layer with organosilicate plates could prevent moisture/alkali contact and reaction with glass lattice at a crack tip (stress corrosion). As aforementioned, the acidic groups of coating molecular interact with or absorb free cations and anions of environment leading to a slow-down of the corrosion process. Secondly, stress-redistribution and crack stopping mechanisms by coatings and nanotube's 'bridging' effect and interface debonding/plastic deformation around crack tip. The mechanical 'healing' effect was viewed as a disappearance of the severe surface flaws because of an increase of the crack tip radius, the flaw filled by coatings being either elliptical than sharp. Thirdly, compressive stress on fiber surface might prevent crack opening/propagation by the shrinkage of polymer due to solidification. As schematically shown in Fig. 4, solidification of coating polymers is accompanied by shrinkage as liquid evaporation (solvent removal) and curing (chemical reaction) occurs, which generates a tensile stress within the polymer layer and a compressive stress within the surface of substrate. Because of the compression closing surface flaw, the strengthening can be increased by increasing the magnitude of the compressive stress [25]. Stress development in drying coatings and explanations for the different stress levels measured for the various polymers can be found elsewhere [26]. Throughout most of a coating, the stress is solely in-plane tensile stress, at edges and inclusions of nanoparticles, more complex concentrations of stress arise and its effect on the efficiency of flaw healing need further investigation.

To simplify the complex phenomena, we developed a simple mechanical model based on Griffith fracture mechanics to roughly estimate the strength of coated fiber [15]. Consider a smoothly coated fiber loaded in tension and having a thin circumferential crack (Fig. 5). When the crack appears, the strain energy is released in a material volume adjacent to the

crack. Assume that this volume is comprised by a conical ring whose generating lines are shown by broken lines and heights are proportional to the crack length. The present assumption is arbitrary and significant analogy to the original Griffith strain energy analysis for an elliptical, sharp crack embedded in a flat, brittle sheet [27] and the accordingly adoption model by incorporating the 3D nature of fiber without consideration of surface coatings [28]. Accordingly, the energy is consumed by formation of new surfaces and deformation of coatings because of an elastic constraint. According to the energy balance, the coated fiber strength, $_f$, can be expressed as

$$\sigma_f > \overline{\sigma}_f = \sqrt{\frac{2\gamma E_f}{(\beta a^* - \frac{L(1+L/d)E_c}{E_f})}} \quad (3)$$

where is fracture surface energy and (=1-2*a**/3d) is a constant coefficient of proportionality which is very close to one since an apparent crack length *a** is much less than fiber diameter *d*. We used the apparent crack length *a** instead of *a* to take into account geometrical influences to surface defect arising from either coatings filling of crack tip or surface roughness. E_f and E_c are Young's modulus of fiber and coatings, respectively. Notably, the critical tensile stress of fiber with a surface flaw, $\overline{c}_f$, is significantly affected by the coating modulus and thickness. Here, we propose a nondimensional healing efficiency factor, = $L(1+L/d)E_c/\ a^*E_f$ as indication of whether the fiber is sufficiently coated and how the reinforcement effect is degraded by environmental corrosion. By applying Eq. 3, therefore, the strength improvement ratio, , can be related to a healing efficiency factor, , as

$$\eta = \frac{c_f - c_o}{\sigma_o} = \frac{1}{\sqrt{1-\varphi}} - 1 \quad (4)$$

where $_o = (2\ E_f / a^*)^{1/2}$ is the strength of fiber without coatings. More rigorous analysis shows that reducing *a** to equilibrium interatomic distance, a_o, of atoms at force equal to zero, $_o$ approaches the ultimate theoretical strength of fiber, $_{max} = E_f /2$. The healing efficiency factor ranges from zero to one representing conditions from non-coating/poor healing case until efficiently healing case. Overall, our glass fibers with nanotube coatings show the highest and mechanical strength improvement (Fig. 5). Generally speaking, the thicker the coating layer and larger the stiffness of coatings the higher is and tensile strength of the fiber. On the other hand, the larger the size of defect and higher the stiffness of fiber, for effective repairing, the thicker and stiffer coatings are required. It implies that the higher strength can be achieved for fiber with surface defect when the healing efficiency factor is more close to one. Moreover, the variation of healing efficiency factor indicates how strong the resistance of the coatings subjected to environmental attack, i.e., no significant reduction of for

nanoclay coatings after alkaline treatment represents its high environmental barrier and anti-corrosion property. Finally, the model allows to estimate approximately the coating stiffness based on the tensile strength of fiber. Taking as estimate E_f = 70 GPa, = 1.75 J/m^2 for glass [29], and average L = 600 nm for the coatings, we can calculate E_c to be 9 GPa for nanotube coatings and 6 GPa for clay coatings, respectively. These values are reasonably consistent with the calculated theoretical values by rule of mixture (ROM), which are 8 GPa and 3 GPa, respectively, for the two corresponding nanocomposite coatings. Further research is required to the adoption of the present model by incorporating the 3D nature of fiber with micro and nano scale dimension within a framework of two-scale numerical finite element investigations.

3.3 Fiber bending strength

To substantiate further the role of nanocoatings in mechanical improvement, we carried out single fiber loop bending test. Fig. 6a shows an example of the shape of a ARG fiber, in which the radius of curvature at failure was measured, also shows the fracture surfaces of a fiber observed by the AFM phase imaging. The AFM scans show a variety of features of fracture phenomena from nanometre to micrometer scale, where a representative fracture mirror, mist, hackle, and branching pattern on a fracture surface can be observed. It is well known that the crack front initially produces the smooth mirror region. As the crack accelerates it becomes more unstable, creating a dimpled surface known as mist. This instability eventually causes the crack to branch out, producing the rough hackle region. The hackle region is characterized by elongated markings that proceed in the direction of crack propagation and the hackle markings point back to the flaw origin on the edges. Based on the highly sensitivity of AFM phase image, we also observed the fine marks in mirror region which point back to the flaw origin in more detail which have not been reported previously. The distance from the fracture origin to the onset of the mist is referred to as the mirror radius. It would be of interest to relate the mirror radius to mist to the magnitude of the stress, , at failure by an empirical relation of the form: = A / $R_m^{1/2}$ [30]. R_m indicates the mirror radius which is about 1.2 m in this sample. A is the empirically derived constant which is 2.1 MPa×m$^{1/2}$ for silica fiber [31]. Therefore, the calculated failure stress is about 1.9 GPa, which is a fairly good agreement with above tensile test measured fiber strength. The verification of the above relationship between stress and mirror radius is important for quantitative fractography. It can be used to estimate the failure stress with good precision over a wide range of applied stresses simply by measuring the mirror radius on a failed component and quantifying the failure stress in this case is critical to determining the location and root cause of the failure event.

The corresponding failure bending moment and the maximum bending stress in the bending test are presented in Fig. 7b. As expected, both values of nanotube coated fibers are higher compared to those of the unsized fibers. Similar to the tensile test, the data scatter in the bending strengths decrease after surface coating, suggesting that the healed flaws on the coated fibers show similar flaw size as aforementioned. It, however, interesting to note that the effect of coating on bending properties leading to an increase of less than 20% seems not as remarkable as on the tensile properties. The most plausible explanation for the behavior is that the maximum stress subjected to tension during bending only involves a small strip surface region at the outside top of the loop compared to all fiber surface area. Only a small fraction of coating, on this region, is in active states for efficient healing. In addition, the gauge length of ~ 0.5 mm in the loop test is considerably shorter than that of 20 mm in the tensile test. In comparison with the case of tensile tests, therefore, only a small fraction of coating, on this small strip region of the relatively short length of fiber, is in active states for efficient healing. In view of statistics, with decreasing efficient specimen surface area to the small strip surface region, the chance of finding a large flaw decreases. Thus, the healing effect for these sub-critical flaws in this region will be less significantly revealed in the loop test. It is also worth to mentioning that the calculated maximum stress at fiber edge is 2.6~3 GPa which is higher than the values of above tensile strength. This is because the measured strength depends on the length/volume of the test fiber. As aforementioned, the gauge length in the loop test is considerably shorter than that in the tensile test, therefore higher strength in loop test is obtained.

3.4 Interfacial adhesion

To investigate whether the nanocoatings could affect interfacial adhesion, we finally tested the both concrete and PP matrix composites with nanocomposite coated ARG and E-glass fibers. In comparison of the systems without clay (see Table 1), the sized fiber with clay shows a significantly higher local interfacial shear strength $_{d}$ and critical interfacial energy release rate G_{ic}. We applied additional polymer coating with clay on the sized fiber which shows the best performance. The exact mechanisms of the improvement in adhesion strength is not clear, but it is generally accepted that the hybrid nanocoatings must influence the interphase adhesion and mechanical properties as well as its size, which in turn influence stress distribution and interfacial fracture behaviour. One recent proposal is that the functionalized carbon material (e.g. CNT or nanocarbon fiber) within the coating is reactive with the reinforcement as well as the matrix material [32, 33]. Besides, the coating with clay results in a much less degradation due to limited access of the aggressive alkali solution, which consequently increase the frictional component of bond.

Our approach was further extended for single-walled carbon nanotubes (SWCNTs)/E-glass fiber reinforcements and thermoplastic polypropylene filaments using commingled yarn technologies. The in-situ commingling enables to combine homogeneously both glass and polypropylene filament arrays in one processing step and without fiber damage compared to commingling by air texturing [34]. We found that the local adhesion strength and the critical interface energy release rates are significantly improved for sizings with SWCNTs system. Regarding the fracture surface after pull-out, it is interesting that some small coarse texture can be observed for SWCNTs system and its roughness is increased (Fig. 8), which is likely to involve mechanical interlinking (anchor effect) of carbon nanotubes against matrix deformation/cracking. We suggest that different nanotube related toughening mechanisms underlie the multi-scale interfacial fracture behaviour, including glass fiber/nanotube/matrix interfacial debonding, nanotube pull-out, and interfacial crack bridging, et al. Additional data are clearly desirable and a more thorough study is required based on a fractal dimension approach [35] to built an energy-geometry link between critical interphase energy release rate by micromechanical testing and detailed fracture surface features.

4. Conclusions

An experimental investigation of nanocomposite coatings for healing surface flaws of glass fibers and improving alkali-resistance was performed. We found that, with low fraction of nanoreinforcements, the nanostructured and functionalised traditional glass fibers show significantly improved both mechanical properties and environmental corrosion resistance. The most remarkable mechanical strength improvement is found for glass fibers with nanotube coatings, corresponding to the highest healing efficiency factor. Our study reveal that the coating modulus, thickness and roughness are responsible for the mechanical enhancement. No apparent strength variation appears for nanoclay coated fiber subjected to alkaline attack, which indicates that the influence of moisture solvent uptake and concentration on mechanical properties decreases when the organoclay is dispersed in coating polymer. Besides, nanocomposite coatings result in higher fiber/matrix interfacial adhesion, suggesting nanotube related interfacial toughening mechanisms. Overall, the hybrid nanocoatings cause improved fiber strength, corrosion resistance, and interfacial properties.

References

1. Gao SL, Mäder E, Abdkader A, Offermann P. Sizings on alkali-resistant glass fibers: environmental effects on mechanical properties. Langmuir 2003;19:2496-506.

2. Gao SL, Mäder E, Plonka R, Liu JW. Surface flaw sensitivity of glass fibers with nanoreinforcement in polymer coating. In: Proc. 15th Intern. Conf. Compos. Mater. (ICCM-15), Durban, South Africa; July 2005.
3. Vigolo B, Penicaud A, Coulon C, Sauder C, Pailler R, Journet C,et al. Macroscopic fibers and ribbons of oriented carbon nanotubes. Science 2000;290:1331–4.
4. Ericson LM, Fan H, Peng HQ, Davis VA, et al. Macroscopic, neat, single-walled carbon nanotube fibers. Science 2004;305:1447-50.
5. Zhao B, Mönch I, Vinzelberg H, Mühl T, Schneider CM. Spin-coherent transport in ferromagnetically contacted carbon nanotubes. Appl Phys Lett 2002;80:3144-6.
6. Mönch I, Leonhardt A, Meye A, Hampel S, Kozhuharova-Koseva R, Elefant D, Wirth MP, Büchner B. Synthesis and characteristics of Fe-filled multi-walled carbon nanotubes for biomedical application. J Phys 2007;61:820–4.
7. Cleveland JP, Anczykowski B, Schmid AE, Elings VB. Energy dissipation in tapping-mode atomic force microscopy. Appl Phys Lett 1998;72:2613-5.
8. Magonov SN, Elings V, Whangbo MH. Phase imaging and stiffness in tapping-mode atomic force microscopy. Surf Sci 1997;375:385-391.
9. Gao SL, Mäder E. Characterization of interphase nanoscale property variations in glass fiber reinforced polypropylene and epoxy resin composites. Composites A 2002;33:559–76.
10. Eitel W, Oberlies F. Einige Eigenschaften des Glasfadens. Glastechn. Bet. 15 Jahrg. 1937;6:228-31.
11. Zhandarov S, Pisanova E, Mäder E. Is there any contradiction between the stress and energy failure criteria in micromechanical tests? Part II. Crack propagation: Effect of friction on force-displacement curves. Compos Interface 2000;7:149–75.
12. Charlier JC, Iijima S, Growth mechanisms of carbon nanotubes, in carbon nanotubes: synthesis, structure, properties and application. Smalley RE (ed). 2001;80:55-80.
13. Wang YH, Chiu SC, Lin KM, Li YY, Formation of carbon nanotubes from polyvinyl alcohol using arc-discharge method. Carbon 2004;42:2535–41.
14. Yu GJ, Gong JL, Wang S, Zhu DZ, He SX, Zhu ZY, Etching effects of ethanol on multi-walled carbon nanotubes. Carbon 2006;44:1218–24.
15. Gao SL, Mäder E, Plonka R. Nanostructured coatings of glass fibers: Improvement of alkali resistance and mechanical properties. Acta Materialia 2007;55:1043–52.
16. Yano K, Usuki A, Okada A, Kurauchi T, Kamigaito O. Synthesis and properties of polyimide–clay hybrid. J Polym Sci Part A 1993;31:2493–8.
17. Lan T, Kaviratna PD, Pinnavaia TJ. On the nature of polyimide-clay hybrid composites. Chem Mater 1994;6:573–5.

18. Nielsen LE. Models for the permeability of filled polymer systems. J Macromol Sci Chem 1967;A1:929–42.
19. Gusev AA, Lusti HR. Rational design of nanocomposites for barrier applications. Adv Mater 2001;13:1641-3.
20. Fredrickson GH, Bicerano J. Barrier properties of oriented disk composites. J Chem Phys 1999;110:2181-8.
21. Kim JK, Hu CG, Woo RSC, Sham ML. Moisture barrier characteristics of organoclay–epoxy nanocomposites. Compos Sci Tech 2005;65:805–13.
22. Gao SL, Mäder E, Plonka R. Coatings for fiber and interphase modification in a cementitious matrix. Acta Materialia 2004;52:4745-55.
23. Zinck P, Mäder E, Gerard JF. Role of silane coupling agent and polymeric film former for tailoring glass fiber sizings from tensile strength measurements. J Mater Sci 2001;36:5245 – 52.
24. Kosmulski M, Dahlsten P. High ionic strength electrokinetics of clay minerals. Colloid Surf A Physicochem Eng Asp 2006;291:212-8.
25. Green DJ. Compressive surface strengthening of brittle materials, J Mater Sci 1984;19: 2165-71.
26. Lei H, Payne JA, Mccormick AV, Francis LF, Gerberich WW, Scriven LE. Stress development in drying coatings. J Appl Polym Sci 2001;81:1000–13.
27. Griffith AA. The phenomenon of rupture and flow in solids. Phil Trans Roy Soc. A221, 1920.
28. Vasiliev VV, Morozov EV. Mechanics and analysis of composite materials. ISBN: 0-08-042702-2, Elsevier Science Ltd, 2001.
29. Lawn BR. Fracture of brittle solids. 2nd edn, Cambridge Univ. Press: Cambridge, 1993.
30. Shand EB. Breaking stress of glass determined from dimension of fracture mirrors. J Amer Ceram Soc 1959;42:474-7.
31. Mecholsky JJ. Fracture surface analysis of optical fibers. Ceramics and Glasses of the Engineered Materials Handbook, Vol. 4, pp. 663-668, ASM International, 1991.
32. Neema S, Salehi-Khojin A, Zhamu A, Zhong WH, Jana S, Gan YX. J Colloid Interface Sci 2006;299:332-41.
33. Salehi-Khojin A, Stone JJ, Zhong WH. Improvement of interfacial adhesion between UHMWPE fiber and epoxy matrix using functionalized graphitic nanofibers. J Compos Mater 2007;41:1163-76.
34. Mäder E, Rothe C, Brünig H, Leopold T. Online spinning of commingled yarns - equipment and yarn modification by tailored fiber surfaces. Key Eng Mater 2007;334-335:229-32.

35. Gao SL, Mäder E, Zhandarov S. Carbon fibers and composites with epoxy resins: Topography, fractography and interphases. Carbon 2004;25:515-29.

Table 1. Local interfacial shear strength, $_d$, and critical interfacial energy release rate, G_{ic}, of ARG fiber reinforced cement and PP matrix composite

Fiber/Matrix	$_d$ (MPa)	G_{ic} (J/m^2)
ARG Control/Cement	23	0.6
ARG Coating C2/Cement	25	0.7
ARG S1+Clay/Cement	34	2.2
ARG S1+Coating K+Clay/Cement	57	5.7
E-glass PP sizing/PP	22	14.0
E-glass PP sizing+SWCNTs/PP	30	31.8

FIGURE CAPTIONS

Fig. 1. Schematics of nanostructed coatings with nanotube/layered silicate polymer network on glass fiber surface to enhance flaw healing effect and corrosion resistance. The inserts show polymer/MWCNT network by SEM and individual surface functionalized nanotube structure by TEM.

Fig. 2. AFM topography (left) and phase (right) images of nanostructured coating with nanotubes and -APS/epoxy film former sizing on ARG fiber surface.

Fig. 3. (a) Effect of the nanostructed coatings with low fraction of nano-reinforcements on the tensile strength of ARG before and after alkaline treatment in 5 wt% NaOH aqueous solution for seven days in an ambient environment. (b) Weibull plots of fiber fracture probability. Error bars represent standard deviations for the estimate of the mean strength of fifty samples.

Fig. 4. Schematic solidification of coating ploymers accompanied by shrinkage on glass fiber with a surface flaw.

Fig. 5. A sketch of a coated fiber with a surface flaw. The fiber is loaded in tensile stress s and the circumferential surface flaw of length a serves as an initial crack. The fiber diameter and coating thickness are given by d and L, respectively, where a and L are much less than d.

Fig. 6. Response of strength variation ratio to healing efficiency factor .

Fig. 7. Bending properties of ARG fibers: (a) shape of ARG fiber during the loop test and AFM phase image of its failure cross-section. (b) effect of the nanostructed coatings with low fraction of nano-reinforcements on the failure bending moment and maximum stress of ARG fibers. Error bars represent standard deviations for the estimate of the mean values of fifteen samples.

Fig. 8. AFM topography images of fracture surfaces of a) E-glass fibers without SWCNTs and b) E-glass fibers with SWCNTs in sizing after fiber pull-out test (x, y =1 μm, z = 40 nm).

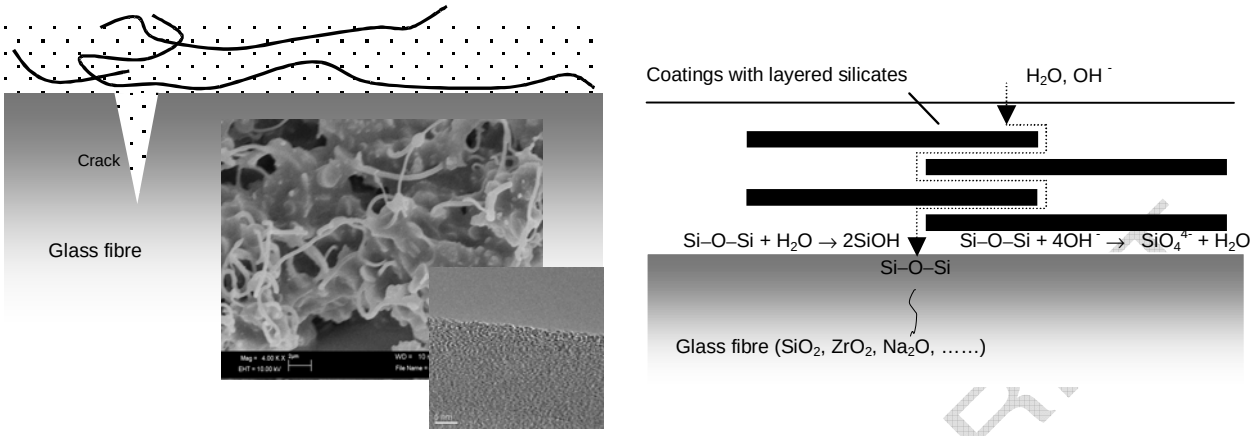

Fig. 1. Schematics of nanostructed coatings with nanotube/layered silicate polymer network on glass fiber surface to enhance flaw healing effect and corrosion resistance. The inserts show polymer/MWCNT network by SEM and individual surface functionalized nanotube structure by TEM.

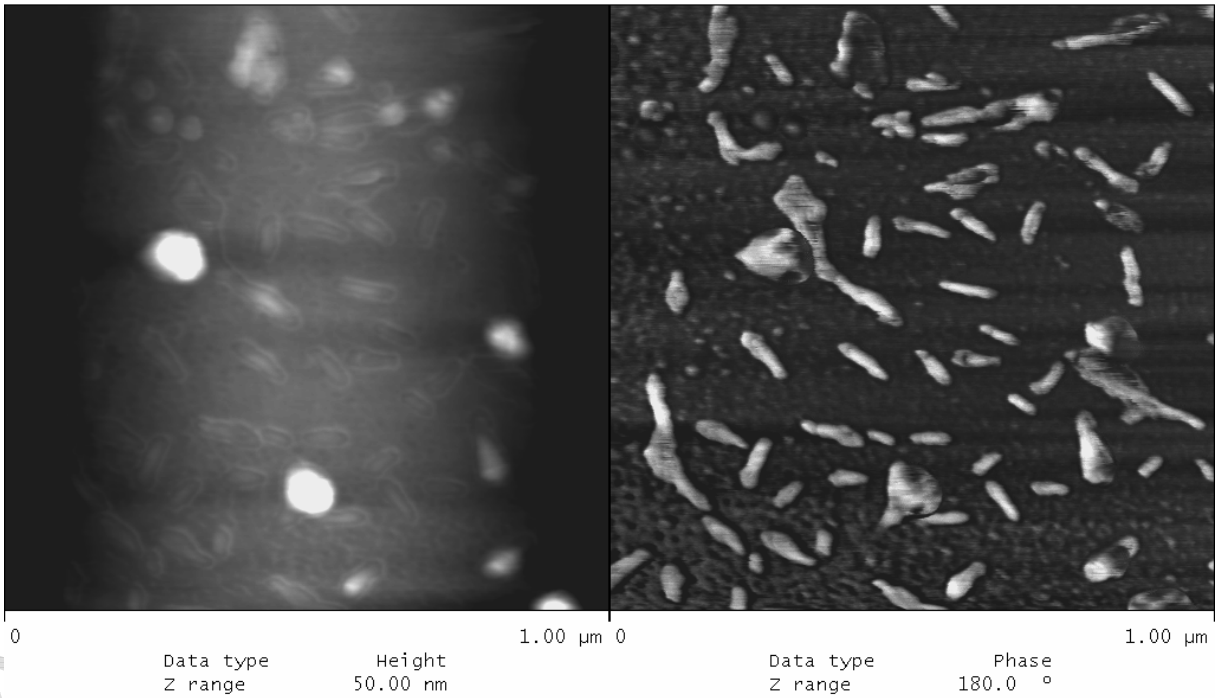

Fig. 2. AFM topography (left) and phase (right) images of nanostructured coating with nanotubes and -APS/epoxy film former sizing on ARG fiber surface.

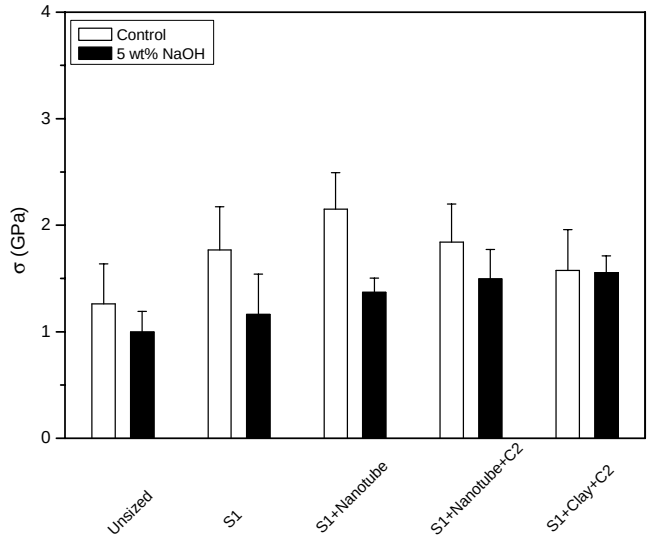

(a)

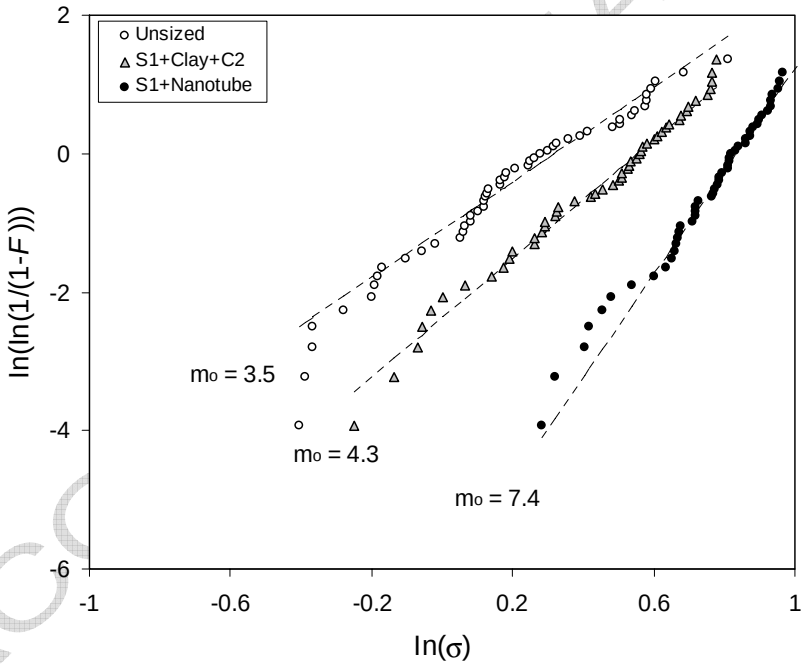

(b)

Fig. 3. (a) Effect of the nanostructed coatings with low fraction of nano-reinforcements on the tensile strength of ARG before and after alkaline treatment in 5 wt% NaOH aqueous solution for seven days in an ambient environment. (b) Weibull plots of fiber fracture probability. Error bars represent standard deviations for the estimate of the mean strength of fifty samples.

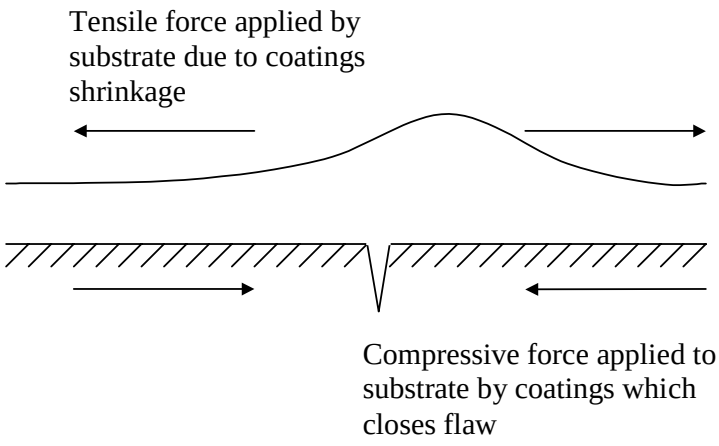

Fig. 4. Schematic solidification of coating ploymers accompanied by shrinkage on glass fiber with a surface flaw.

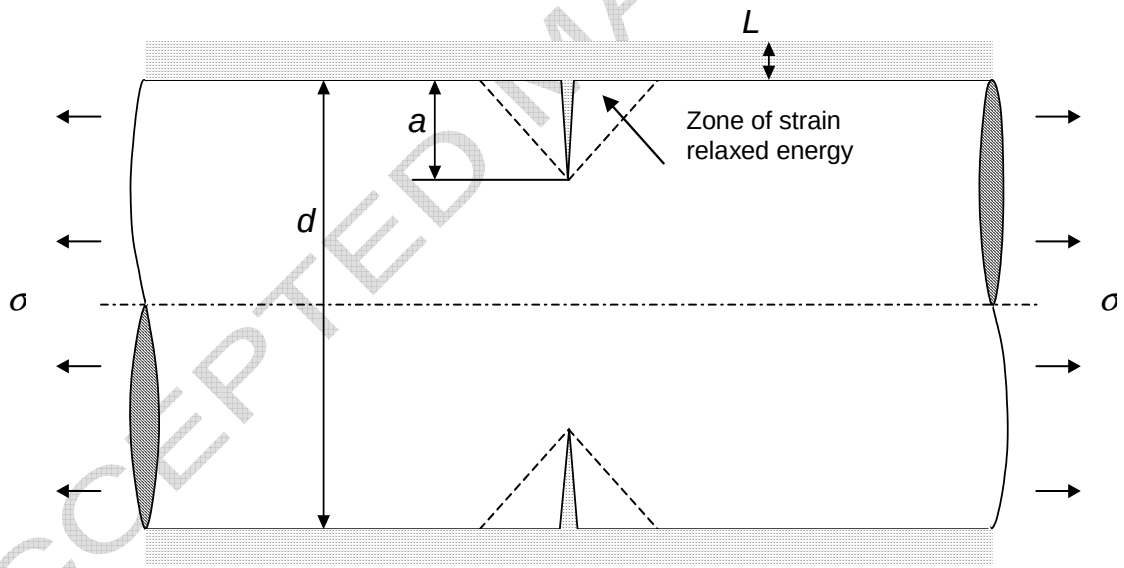

Fig. 5. A sketch of a coated fiber with a surface flaw. The fiber is loaded in tensile stress and the circumferential surface flaw of length *a* serves as an initial crack. The fiber diameter and coating thickness are given by *d* and *L*, respectively, where *a* and *L* are much less than

d.

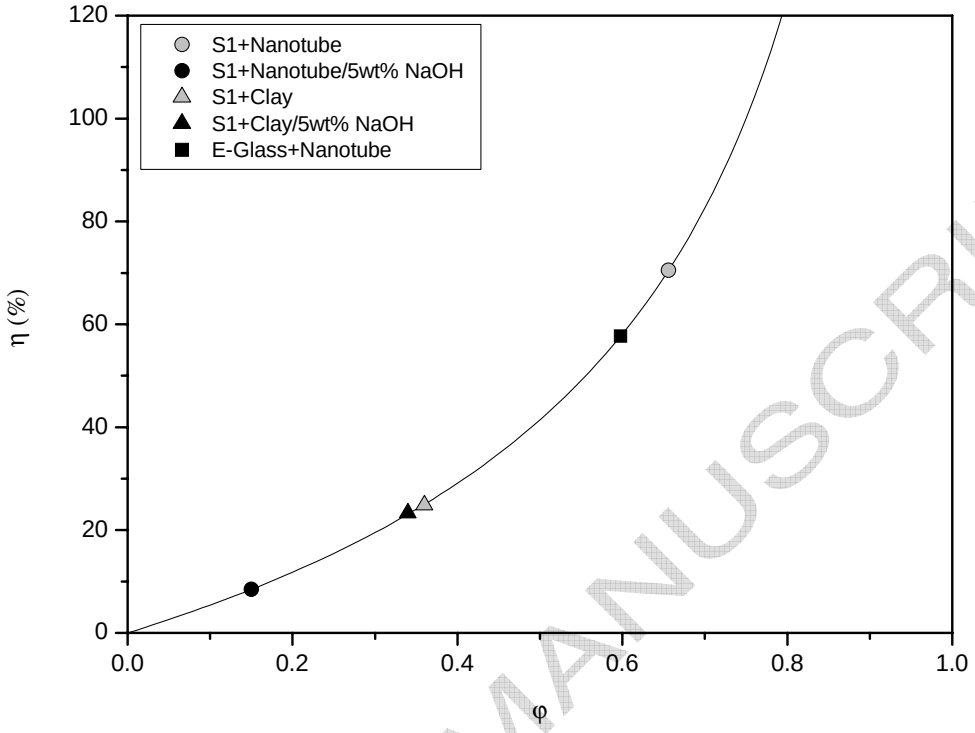

Fig. 6. Response of strength variation ratio to healing efficiency factor .

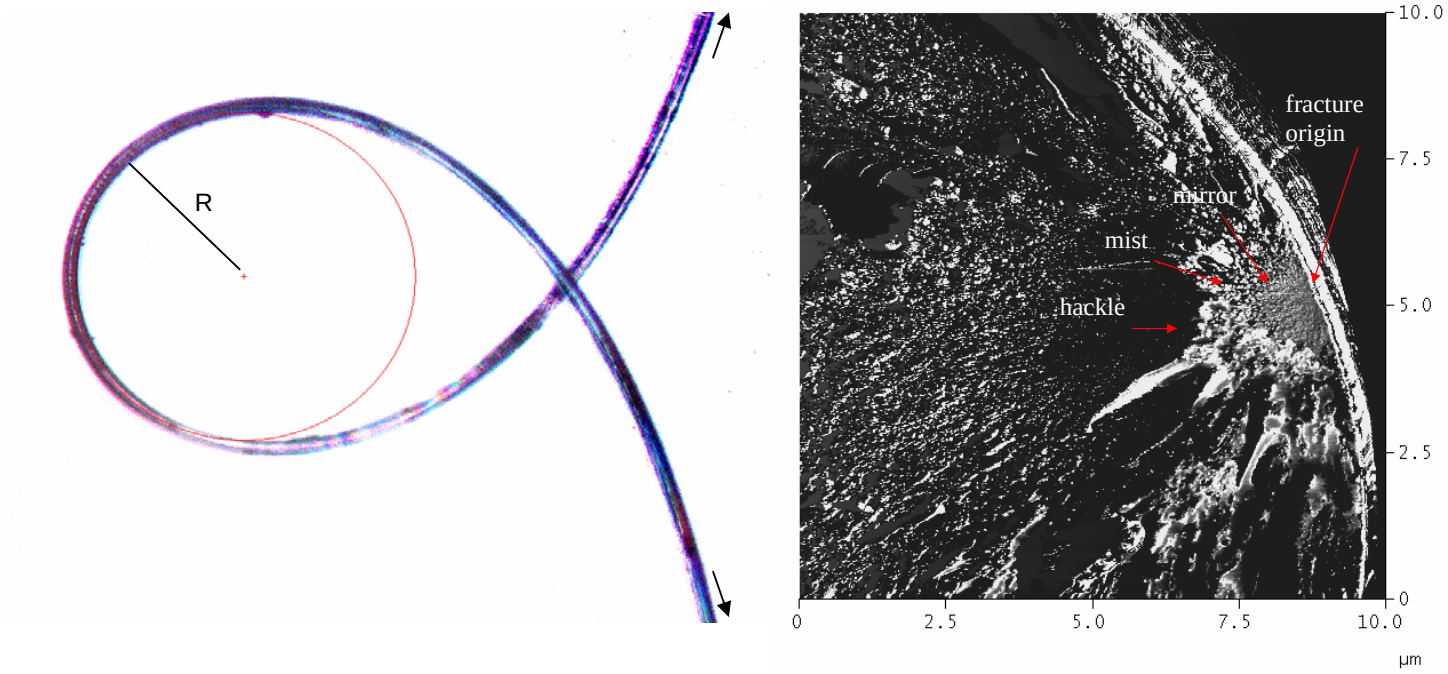

(a)

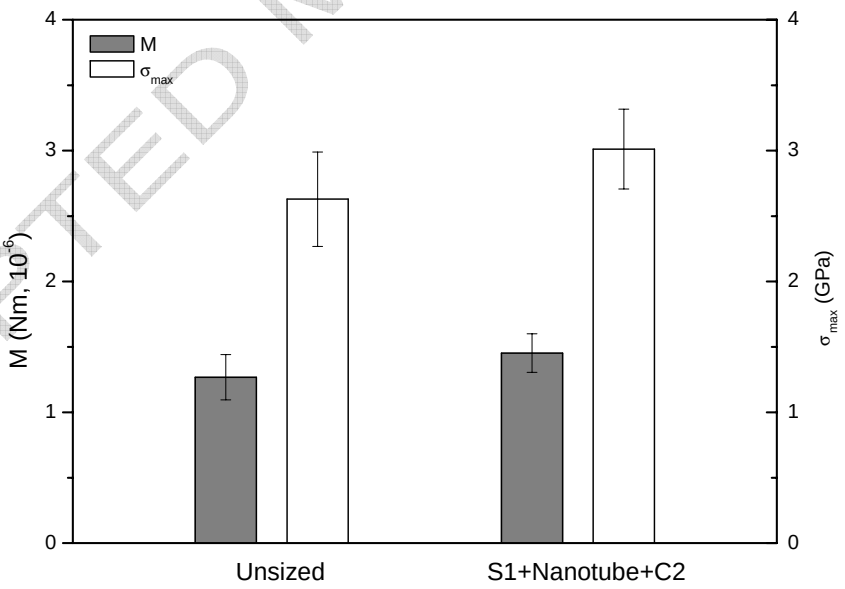

(b)

Fig. 7. Bending properties of ARG fibers: (a) shape of ARG fiber during the loop test and AFM phase image of its failure cross-section. (b) effect of the nanostructed coatings with low fraction of nano-reinforcements on the failure bending moment and maximum stress of ARG fibers. Error bars represent standard deviations for the estimate of the mean values of fifteen samples.

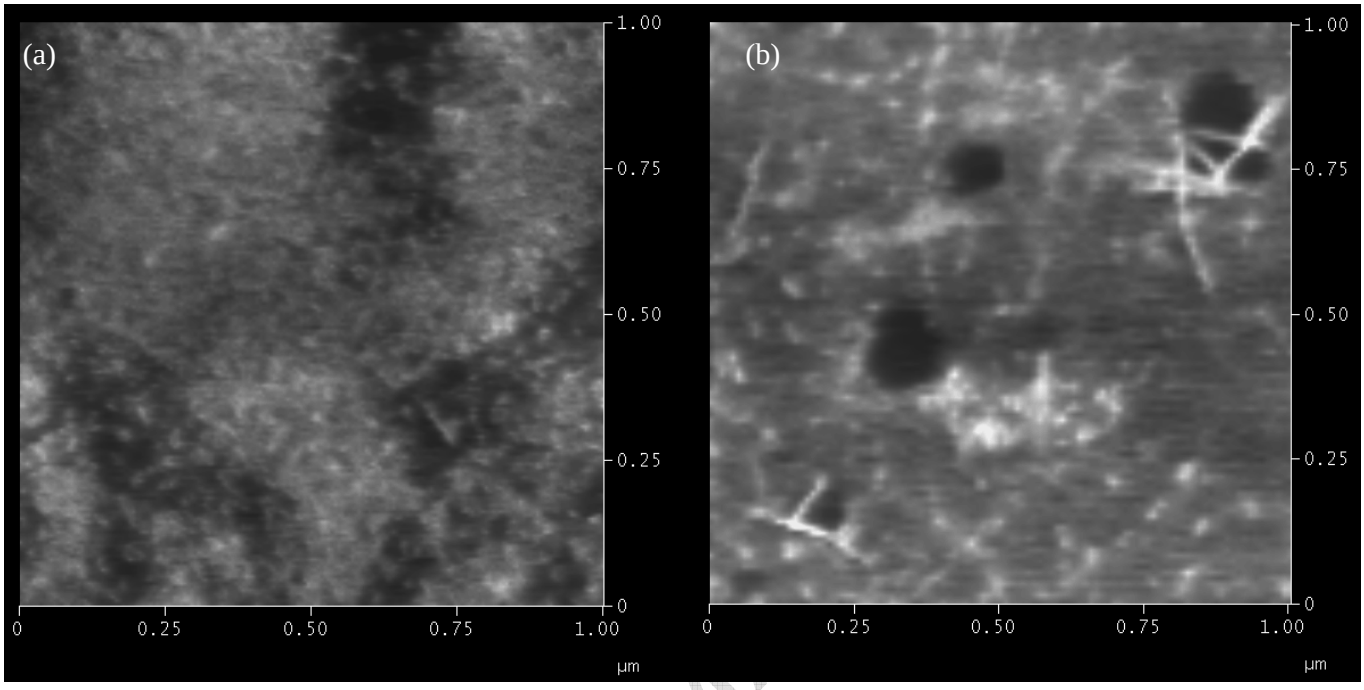

Fig. 8. AFM Phase images of fracture surfaces of a) E-glass fibers without SWCNTs and b) E-glass fibers with SWCNTs in sizing after fiber pull-out test (x, y =1 µm, z = 100°).